# Enhanced Magnon Thermal Transport in Yttrium-doped Spin Ladder Compounds $Sr_{14-x}Y_xCu_{24}O_{41}$

Shuchen Li,[1,*] Shucheng Guo,[1,*] Yitian Wang,[1] Hongze Li,[2] Youming Xu,[1] Veronica Carta,[3] Jianshi Zhou,[2] Xi Chen[1,a)]

[1]Department of Electrical and Computer Engineering, University of California, Riverside, California 92521, United States

[2]Materials Science Program, Mechanical Engineering, The University of Texas at Austin, Austin, Texas 78712, United States

[3]Department of Chemistry, University of California, Riverside, California 92521, United States

[*]These authors contributed equally.

[a)]**Author to whom correspondence should be addressed:** xichen@ucr.edu

## ABSTRACT

Magnons are quasiparticles of spin waves, carrying both thermal energy and spin information. Controlling magnon transport processes is critical for developing innovative magnonic devices used in data processing and thermal management applications in microelectronics. The spin ladder compound $Sr_{14}Cu_{24}O_{41}$ with large magnon thermal conductivity offers a valuable platform for investigating magnon transport. However, there are limited studies on enhancing its magnon thermal conductivity. Herein, we report the modification of magnon thermal transport through partial substitution of strontium with yttrium (Y) in both polycrystalline and single crystalline $Sr_{14-x}Y_xCu_{24}O_{41}$. At room temperature, the lightly Y-doped polycrystalline sample exhibits 430% enhancement in thermal conductivity compared to the undoped sample. This large enhancement can be attributed to reduced magnon-hole scattering, as confirmed by the Seebeck coefficient measurement. Further increasing the doping level results in negligible change and eventually suppression of magnon thermal transport due to increased magnon-defect and magnon-hole scattering. By minimizing defect and boundary scattering, the single crystal sample with x = 2 demonstrates a further enhanced room-temperature magnon thermal conductivity of 19 $W\,m^{-1}K^{-1}$, which is more than ten times larger than that of the undoped polycrystalline material. This study reveals the interplay between magnon-hole scattering and magnon-defect scattering in modifying magnon thermal transport, providing valuable insights into the control of magnon transport properties in magnetic materials.

## I. INTRODUCTION

The collective magnetic excitations in magnetic materials are referred to as magnons, as the quasiparticles associated with spin waves.[1,2] Like phonons, the quasiparticles of lattice vibrations, magnons can propagate in ordered magnetic structures, transporting both thermal energy and spin information. Consequently, magnons can function as heat carriers in some magnetic materials, providing a substantial contribution to thermal transport compared with the conventional heat carriers, phonons and electrons.[3] This ability enables the application of magnon thermal transport in thermal management such as heat dissipation and thermal switching in

microelectronic devices.[4–6] Magnons are also important for the recently discovered spin Seebeck effect,[7] which refers to the generation of a spin voltage caused by a temperature gradient in a magnetic material. The spin Seebeck effect is promising for developing new technologies such as waste heat recovery that converts heat into useable electrical energy.[8] Furthermore, since magnons allow for the transfer of spin angular momentum without the need for charge transport, magnonics are attractive for realizing Joule-heat-free transfer of quantum information.[9–11] To achieve better performance in the applications of thermal management, energy conversion, and magnonics, controlling magnon transport length scale is needed, for which investigating the mechanisms of magnon scattering processes is crucial.[12–16]

The spin ladder compounds $(\mathrm{Sr, Ca, La})_{14}\mathrm{Cu}_{24}\mathrm{O}_{41}$, with a quasi-one-dimensional crystal structure, offer a valuable platform for studying magnon transport, given their large and tunable magnon thermal conductivity ($\kappa_M$).[17–19] The crystal structure of the spin ladder compound $\mathrm{Sr}_{14}\mathrm{Cu}_{24}\mathrm{O}_{41}$ comprises three layers: the $\mathrm{Cu}_2\mathrm{O}_3$ ladder layer, the $\mathrm{CuO}_2$ chain layer, and the Sr ion layer.[20,21] The ladder and chain layers are alternately stacked along the *b*-axis, and are incommensurate along the *c*-axis, while the Sr ions separate the ladder and chain layers. Within the $\mathrm{Cu}_2\mathrm{O}_3$ ladder layer, the $180°$ $\mathrm{Cu}-\mathrm{O}-\mathrm{Cu}$ couplings lead to antiferromagnetic interaction among $\mathrm{Cu}^{2+}$ spins along the *a*- and *c*- axes, serving as the rung and ladder directions, respectively. The strong antiferromagnetic coupling, with $J \approx 170$ meV formed in the ladder layer, leads to a large magnon group velocity of about $10^5\ m\ s^{-1}$, which is about two orders of magnitude larger than the typical sound velocity in solids.[22] Based on the kinetic model,[1] such a remarkable group velocity of magnons is responsible for the large $\kappa_M$. In addition, the singlet-triplet excitation of magnons in spin ladders introduces an energy gap of about 32 meV, which implies that the magnons are frozen at low temperatures and do not contribute to the thermal transport until thermally excited above 50 K.[22–24] Previous thermal conductivity ($\kappa$) measurements on spin ladder compounds have shown a signature double-peak behavior in the temperature-dependent $\kappa$.[17,18,25] The low-temperature $\kappa$ peak at about 50 K is mainly contributed by phonons while the high-temperature peak at about 140 K is attributed to magnons. The difference in peak temperatures of phonon and magnon thermal transport makes it easier to separate the phonon and magnon contributions to $\kappa$ for studying the magnon related properties.

In the spin ladder compounds, magnon thermal transport can be modified by chemical doping. For example, the doping of Ca or La ions can affect the $\kappa_M$ by changing the magnon-hole scattering intensity. In the undoped spin ladder compound $\mathrm{Sr}_{14}\mathrm{Cu}_{24}\mathrm{O}_{41}$, there are a total of 6 $\mathrm{Cu}^{3+}$ ions, considered as holes, per formula unit in the ladder and chain layers to maintain the charge neutrality.[26] These holes are non-magnetic defects and can suppress the magnon thermal transport.[27,28] Due to the difference in the atomic sizes, the substitution of Sr with Ca can reduce the lattice constants and transfer holes from the chain layer to the ladder layer,[29,30] inducing stronger magnon-hole scattering and suppressing $\kappa_M$.[17] On the other hand, La ions have a higher valence state than Sr and Ca ions. La-substitution can reduce the hole concentration in the spin ladder compounds, thereby suppressing magnon-hole scattering and enhancing $\kappa_M$.[17,31,32] Yttrium (Y), similar to La, can substitute Sr in the spin ladder compounds. Its valence state of +3 can reduce the hole concentration, which has been confirmed by previous optical and electrical studies.[26,33] It is expected that the $\kappa_M$ can also be enhanced by Y-doping. Furthermore, chemical doping can induce lattice distortion, thereby intensifying magnon-defect scattering, which may potentially counteract the effect of magnon-hole scattering. However, there is no experimental study on the impact of Y-doping on magnon thermal transport in spin ladder compounds.

In this work, we prepared both polycrystalline and single crystal samples of Y-doped spin ladder compounds, $\mathrm{Sr}_{14-x}\mathrm{Y}_x\mathrm{Cu}_{24}\mathrm{O}_{41}$ ($0 \le x \le 6$), using the solid-state reaction (SSR) and traveling solvent floating zone (TSFZ) methods, respectively. The effects of Y-doping on crystal structure, and electrical and thermal properties of the samples were systematically investigated. The solid-solution limit of Y in spin ladders is found to be x = 4.6. The value of $\kappa_M$ is greatly improved in the lightly Y-doped spin ladder compounds due to the reduced magnon-hole scattering. Further increasing Y-doping level suppresses $\kappa_M$ by overwhelming magnon-defect and magnon-hole scattering, constating with the continuously increasing $\kappa_M$ by La-doping.[34] The Seebeck coefficient ($S$) measurement shows a similar non-monotonic doping-dependent behavior, indicating a close relation between

the hole concentration and the magnon thermal transport. The unchanged two-magnon Raman peak position indicates that Y-doping does not modify the magnon group velocity. Compared with the undoped single crystal, a more than doubled $\kappa_M$ at 300 K was observed in the lightly Y-doped $Sr_{12}Y_2Cu_{24}O_{41}$ single crystal sample. The magnon mean free path $l_M$ was calculated based on a kinetic model to better understand the magnon transport mechanisms in Y-doped samples.

## II. MATERIAL AND EXPERIMENTAL METHODS

### A. Synthesis of polycrystalline and single crystalline samples

The starting materials for $Sr_{14-x}Y_xCu_{24}O_{41}$ were $SrCO_3$ (purity: 99.9%, Sigma-Aldrich), $Y_2O_3$ (purity: 99.99%, Thermo Scientific), and $CuO$ (purity: 99.7%, Thermo Scientific). Polycrystalline samples were synthesized using the SSR method. The starting materials were mixed according to the stoichiometric ratio. The mixtures were sintered at 940 °C for 48 hours, then consolidated into pellets by cold pressing under a pressure of 330 MPa. The obtained pellets were annealed at 940 °C in the air for 12 hours. The single crystalline samples were synthesized by the TSFZ method using a Quantum Design's 2-mirror IR image furnace (model: IRF01-001-05), similar as a previous report.[35] The feed and seed rods were made with the same powders as the polycrystalline samples. The solvent pellets were made with the same starting materials as polycrystalline samples with the atomic ratio of $Cu : (Sr, Y) = 85 : 15$, where the atomic ratio of $Sr : Y$ is equal to that of the feed rod. The TSFZ growth was carried out under an oxygen pressure of 1 bar, with a growth rate of 0.8 mm per hour, and a rotation speed of 30 rpm for feed and seed rods in opposite directions.

### B. Phase and microstructure characterization

The phase purity and crystal structure of the samples were characterized using a PANalytical Empyrean Series 2 X-ray diffraction (XRD) machine with Cu Kα (λ = 1.54 Å) radiation. MDI Jade software was used to analyze the XRD results of the samples. Six strong peaks were selected to calculate the lattice parameters based on Bragg's law.

The microstructure and elemental analysis of the polycrystalline samples were studied by 4 TESCAN Vega3 SBH scanning electron microscopy (SEM) with energy dispersive X-ray spectrometry (EDS). The quality and orientation of the single crystalline samples were characterized by single-crystal XRD with a Bruker D8 Venture equipped with a PhotonIII detector using Mo Kα (λ = 0.71073 Å) IμS micro-source for face indexing. The Laue back reflection study was also performed to check the quality of the single crystalline samples using a Laue modulus on a Philips PW 1830 X-ray generator. The details of the single-crystal XRD and Laue back-reflection study are given in the Supplementary Material. Raman measurement was performed to understand the magnetic couplings in the single crystal samples using the Horiba LabRam with a 532 nm Coherent Sapphire laser at room temperature. The incident laser beam is non-polarized and oriented perpendicular to the *c*-axis of the crystals.

### C. Thermal and electrical measurements

The specific heat $C_p$, thermal conductivity $\kappa$, and Seebeck coefficient $S$ of the samples were measured by Quantum Design's physical property measurement system (PPMS). The measurement of $C_p$ was performed on samples with dimensions of about $1 \times 1 \times 0.5$ mm$^3$ between 3-300 K. $\kappa$ and $S$ were measured through PPMS's continuous mode under a continuous heating rate of 0.3 K min$^{-1}$ in the temperature range of 3-300 K. The

measurements were performed on the bar-shape samples of about $1 \times 1 \times 8\ mm^3$ with a four-probe configuration. The polycrystalline samples were cut along both in-plane (IP) and out-of-plane (OP) directions of the pellets. The single crystal samples were cut parallel and perpendicular to the *c*-axis. The details for the uncertainty analysis of the thermal conductivity measurements are given in the Supplementary Material.

## III. RESULTS AND DISCUSSION

### A. Phase and microstructure of polycrystalline $Sr_{14-x}Y_xCu_{24}O_{41}$

The crystal structure of spin ladder compounds is displaced in Fig 1(a). Y dopants can replace the Sr atoms between the spin ladder sand spin chain layers. As shown in Fig. 1(b), the XRD patterns of $Sr_{14-x}Y_xCu_{24}O_{41}$ polycrystalline samples indicate that the samples are mostly pure after the SSR process as all the major peaks can be indexed as $Sr_{14}Cu_{24}O_{41}$ (PDF#: 48-1496). A small amount of impurities identified as $YCu_2O_4$ and CuO can be observed in the sample with x = 6. Fig. 1(c) shows that the three highest peaks of samples shift to higher angles gradually as x increases. This observation indicates that the lattice constants have been changed when Sr is replaced by Y. Fig. 1(d) shows the obtained lattice constants of various Y-doped samples by refining the XRD patterns, which are compared with a previous study.[36] As the value of x increases, the lattice constant *b* decreases from 13.34 to 12.92 Å while the lattice constants *a* and *c* show negligible change by Y-doping. A linear fitting on the obtained values of *b* shows that the decreasing trend of *b* is different for $4 < x < 6$. Assuming the lattice constant *b* decreases linearly with Y-doping level until reaching a saturation level based on Vegard's law,[37] we found that the solubility limit of Y in $Sr_{14-x}Y_xCu_{24}O_{41}$ is x = 4.6. This result is consistent with the previous studies.[36,38,39]

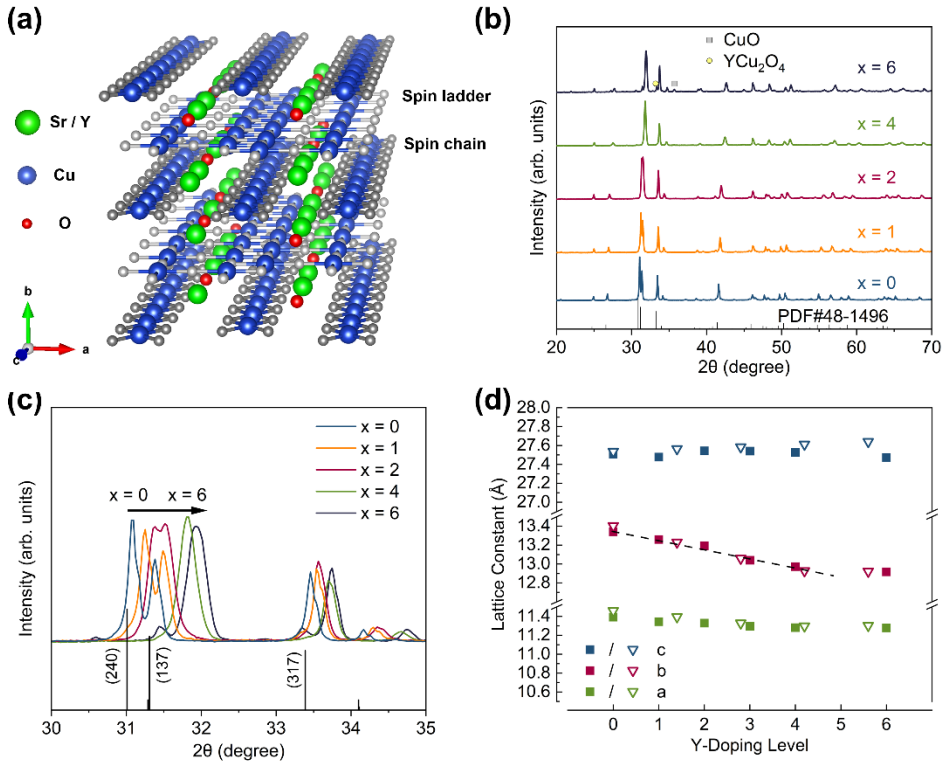


**Fig. 1**. (a) Crystal structure of the spin ladder compounds. (b) The XRD patterns of $Sr_{14-x}Y_xCu_{24}O_{41}$ polycrystalline samples. (c) The XRD patterns of $Sr_{14-x}Y_xCu_{24}O_{41}$ polycrystalline samples with 2θ between 30° to 35°. The arrow shows the direction of peak

shifting with the increasing value of x. (d) The lattice constants of $Sr_{14-x}Y_xCu_{24}O_{41}$ obtained from the XRD analysis, compared with a previous study marked as open symbols.[36]

Fig. 2(a)-(c) present the SEM images of the x = 0, 2, and 4 samples after cold pressing. The average grain sizes are 3.4, 2.7, and 2.1 μm for the samples with x = 0, 2, and 4, respectively. The detailed grain size analysis can be found in Fig. S1 of Supplementary Material. The grain size decreases slightly as the Y-doping level increases, which suggests that the Y-doping can decrease the reaction rate during SSR and cause smaller grain sizes.[39] The EDS mapping results for the sample with x = 4 are illustrated in Fig. 2(e)-(h). All the elements Sr, Y, Cu, and O show a uniform distribution, which indicates a homogeneous distribution of Y in the samples after cold pressing. The atomic ratio of Sr: Y: Cu determined by the EDS is about 10: 3: 22, which is close to the designed ratio of 10: 4: 24.

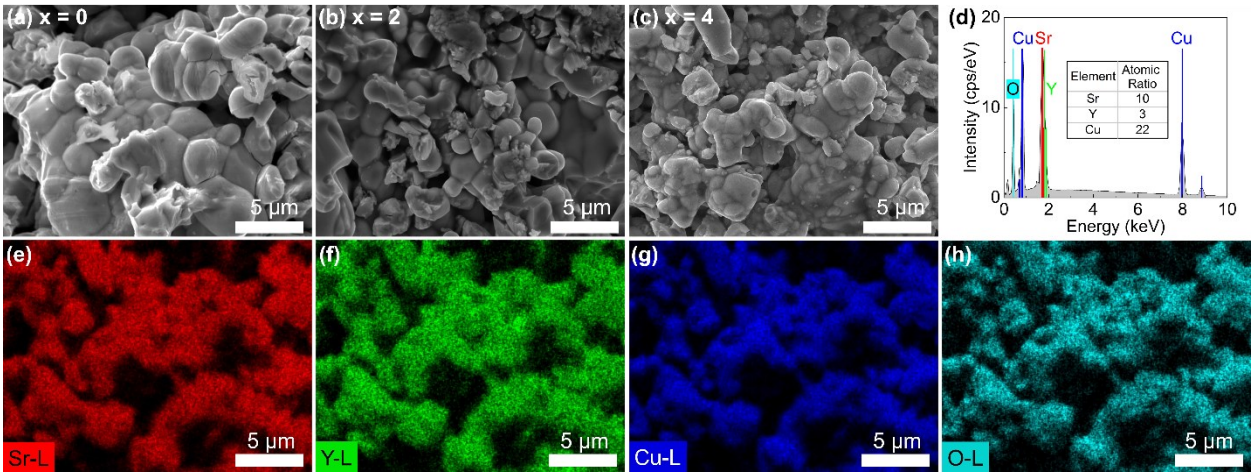


**Fig. 2**. (a-c) SEM images of samples with x = 0, 2, and 4, respectively. (d) EDS spectrum of $Sr_{10}Y_4Cu_{24}O_{41}$. The inset is the EDS element analysis result of Sr, Y, and Cu. (e-h) EDS mapping for Sr, Y, Cu, and O in $Sr_{10}Y_4Cu_{24}O_{41}$, respectively.

### B. Thermal and electrical properties of polycrystalline $Sr_{14-x}Y_xCu_{24}O_{41}$

The measured $\kappa$ data along the IP and OP directions of the polycrystalline samples are shown in Fig. 3(a-b). For all the samples, $\kappa$ measured along the IP direction is higher than that of the OP direction, which is due to the texture effect as reported in previous studies.[15,25,31] The solid thermal conductivity ($\kappa_s$) can be obtained by correcting the porosity effect as discussed in the Supplementary Material. According to a study by Kato *et al.*,[40] the electrical resistivity of the undoped spin ladder compound $Sr_{14}Cu_{24}O_{41}$ monotonically decreases with increasing temperature, reaching approximately 0.001 Ω m at 300 K. Y-doping can further increase the resistivity by several orders of magnitude.[40] Based on the Wiedemann-Franz law, the electron contribution to $\kappa$ for the undoped sample at 300 K is less than 0.008 W $m^{-1}K^{-1}$, which is negligible compared to the total $\kappa$. Since magnons are frozen at low temperatures due to the large energy gap, the low-temperature thermal transport is primarily contributed by phonons.[41] The lattice thermal conductivity ($\kappa_L$) can be obtained by fitting $\kappa_s$ below 50 K using a Callaway model[42] and extrapolating the fitting to high-temperature region. The detailed fitting of $\kappa_L$ can be found in the Supplementary Material. The obtained $\kappa_s$ and $\kappa_L$ are shown in Fig. 3(c) and (d). $\kappa_s$ exhibits a unique behavior in the x = 0 sample compared with the other samples. In this undoped sample, a signature double-peak behavior is observed with the highest peak values of $\kappa_L = 5.2$ W $m^{-1}K^{-1}$ and 4.6 W $m^{-1}K^{-1}$ at 40 K along the IP and OP directions, respectively, which are more than double those of other samples. At 50 K, $\kappa_s$ decreases gradually with increasing x, which indicates an increased phonon-defect scattering due to Y-doping. Furthermore, the x = 2 and 4 samples exhibit high values of $\kappa_s$ above 200 K, where the magnon contribution dominates the total thermal transport.

Since the magnon thermal transport in the polycrystalline samples is uniform along the IP direction, the intrinsic $\kappa_M$ is obtained as: $\kappa_M = 2\kappa_{M,\mathrm{IP}} + \kappa_{M,\mathrm{OP}} = 2(\kappa_{s,\mathrm{IP}} - \kappa_{L,\mathrm{IP}}) + (\kappa_{s,\mathrm{OP}} - \kappa_{L,\mathrm{OP}})$.[25] The factor of 2 in the expression is due to one-dimensional magnon transport, which needs to be summed over the two IP directions and one OP direction to get $\kappa_M$ for a polycrystal. As shown in Fig. 4(a), the sample with x = 0 displays a peak in $\kappa_M$ around 160 K, whereas samples with x = 2, 4, and 6 demonstrate a continuous increase in $\kappa_M$ up to the measured temperature. This observation can be attributed to decreased magnon scattering by Y-doping near room temperature. Furthermore, the $\kappa_M$ value near 300 K increases initially with Y-doping content up to x = 4. Further increasing the Y content results in a suppression of $\kappa_M$. Above 150 K the x = 2 and 4 samples show large $\kappa_M$, which is about 6.4 W $\mathrm{m^{-1}K^{-1}}$ at 300 K. This value is more than 430% larger than that of the x = 0 sample. Our observation indicates a non-monotonic Y-doping effect on the magnon scattering processes in the spin ladder compounds. Other than the magnon-defect scattering, the Y-doping effect also engages in other magnon scattering mechanisms that improve $\kappa_M$ in $Sr_{14-x}Y_xCu_{24}O_{41}$. As Y-doping can reduce the hole concentration in the spin ladder compound,[33] we believe that the enhancement of $\kappa_M$ results from suppressed magnon-hole scattering, which will be discussed in detail below.

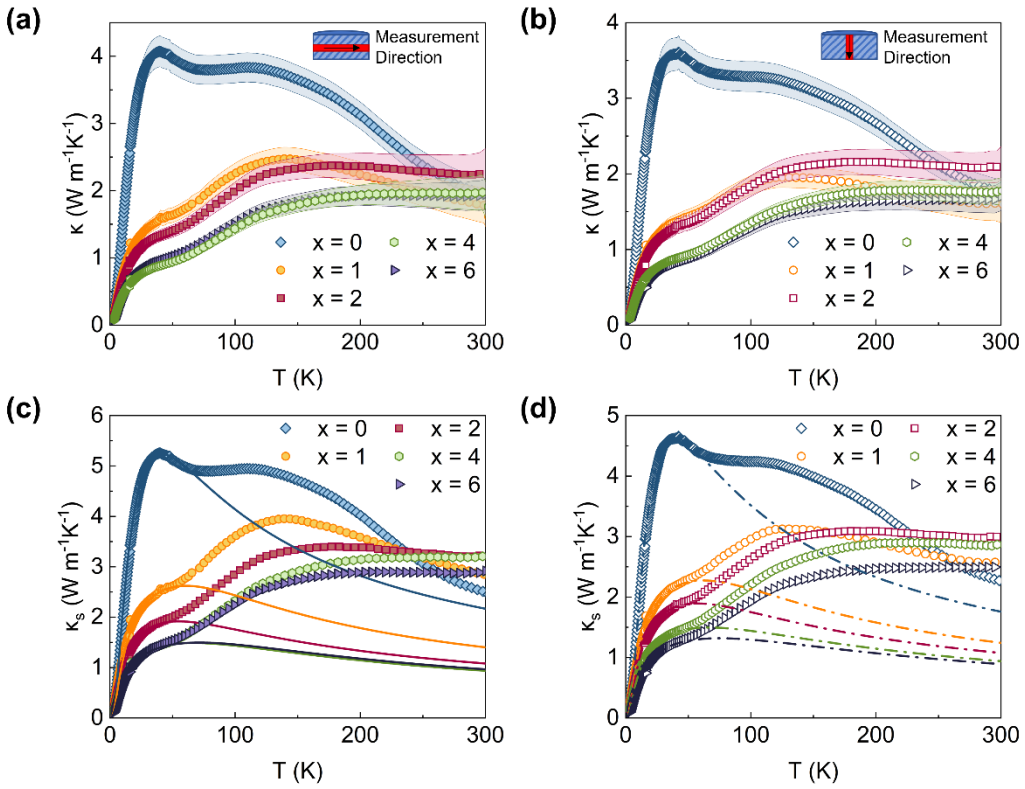


**Fig. 3**. (a), (b) $\kappa$ of $Sr_{14-x}Y_xCu_{24}O_{41}$ polycrystalline samples along IP and OP directions, respectively. The shaded area presents the measurement uncertainty. (c) $\kappa_s$ and (d) $\kappa_L$ of $Sr_{14-x}Y_xCu_{24}O_{41}$ polycrystalline samples along IP and OP directions, respectively.

To better understand the effect of Y-doping on $\kappa_M$, magnon mean free path $l_M$ is calculated as:[43]

$$l_M = \kappa_M \left( \frac{3n_s}{\pi \hbar k_B T^2} \int_{\Delta}^{\epsilon_{max}} \frac{\exp\left(\frac{\epsilon}{k_B T}\right)}{\left[\exp\left(\frac{\epsilon}{k_B T}\right) + 3\right]^2} \epsilon^2 d\epsilon \right)^{-1} \quad (1)$$

where $\hbar$ is the reduced Planck constant, $k_B$ is the Boltzmann constant, $n_s$ is the number of spin ladders per unit cross-sectional area perpendicular to the spin ladders, $T$ is the temperature, $\Delta$ is the energy gap of the magnon

dispersion of ladders, and $\epsilon_{max}$ is the band maximum of the spin excitations of ladders. In this analysis, the values of Δ and $\epsilon_{max}$ are chosen to be 32.5 and 200 meV, respectively, according to a previous report.[22] The obtained $l_M$ decreases with increasing temperature, as plotted in Fig. 4(b). Below about 160 K, $l_M$ is increased for the samples with x = 1 and 2, which can be attributed to the suppressed magnon-hole scattering by Y-doping, while $l_M$ is reduced if the doping concentration is further increased due to enhanced defect scattering. The sample with x = 6 shows an even lower $l_M$ as compared to the undoped sample. In contrast, $l_M$ shows a different non-monotonic doping dependence at 300 K, the maximum value of $l_M$ appears in the x = 2 and 4 samples, with a value of about 40 Å. Further increasing the Y content to x = 6 leads to a slightly reduction of $l_M$, which is still larger than that of undoped sample. Our observations suggest that magnon-defect scattering is a significant scattering mechanism below approximately 160 K, whereas magnon-hole scattering becomes more important at higher temperatures. In addition, the maximum value of $l_M$ for the x = 0 sample is only about 140 Å at 100 K, which equivalent to about 5 unit cells along *c*-axis and much smaller than the average grain size. This result implies a high defect concentration in the polycrystalline samples. Since magnon-defect scattering is dominant at low temperatures, the effect of grain size on magnon thermal transport becomes negligible, as reported in a previous study.[31]

The averaged lattice thermal conductivity can be calculated as $\kappa_L = (2\kappa_{L,IP} + \kappa_{L,OP})/3$. The obtained average $\kappa_L$ data are displayed in Fig. 4(c). The phonon mean free path ($l_p$) can be calculated using a kinetic model as:[42]

$$l_p = \kappa_L \left( \frac{{k_B}^4 T^3}{2\pi^2 v_s^2 \hbar^3} \int_0^{\frac{\theta_D}{T}} \frac{x^4 e^x}{(e^x-1)^2} dx \right)^{-1} \quad (2)$$

where $v_s$ is the sound velocity, $\theta_D$ is the Debye temperature, and $x = \frac{\hbar\omega}{k_B T}$, which acts as a variable of integration. Fig. 4(d) shows a monotonic decrease of $l_p$ with the increasing value of x, especially in the temperature range of ~10-30 K. This finding is mainly caused by the enhanced defect scattering of phonons by Y-doping in the intermediate temperature range while the boundary scattering is dominant below 10 K.[44]

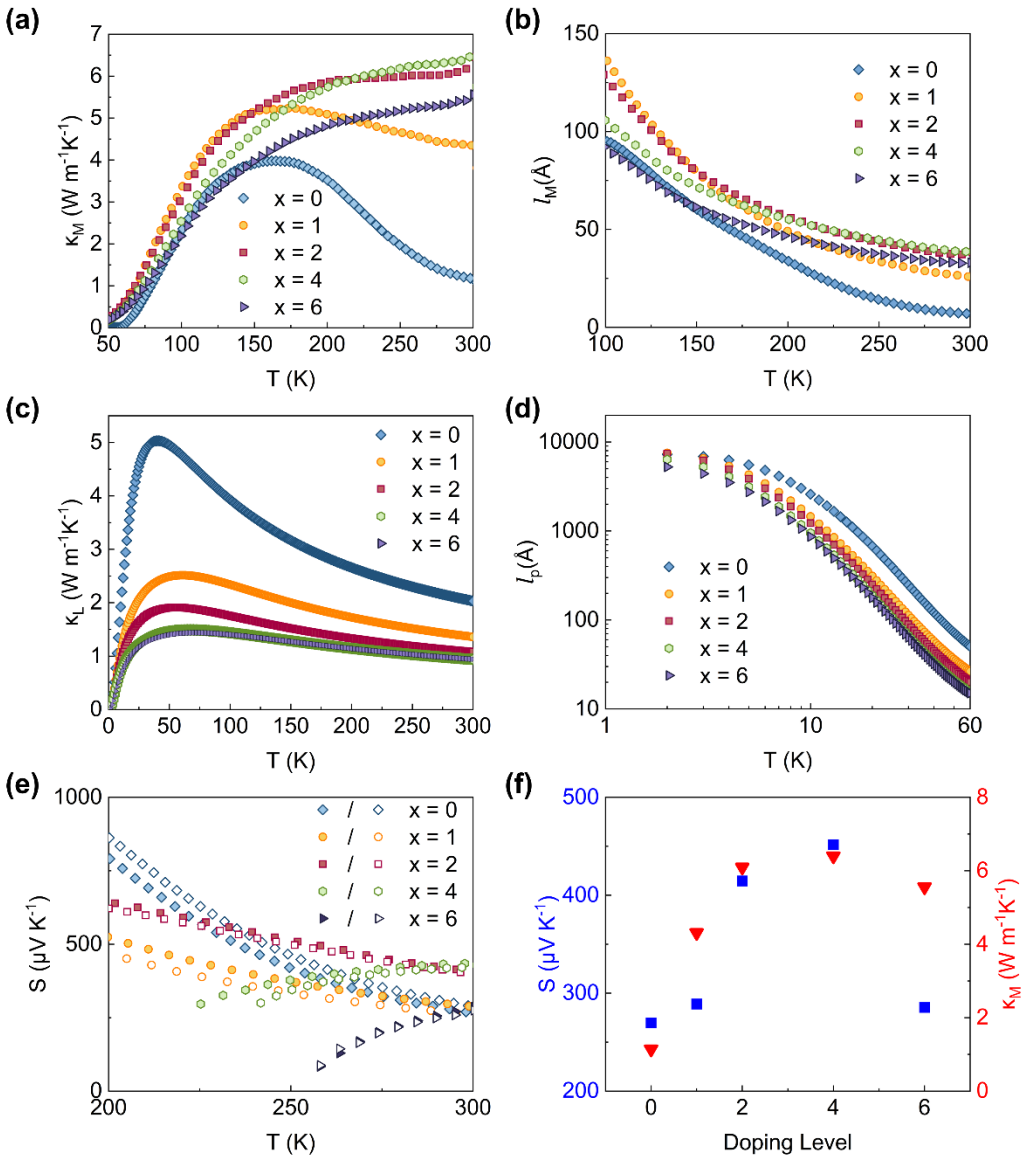


**Fig. 4**. (a) $\kappa_M$ and (b) $l_M$ of $Sr_{14-x}Y_xCu_{24}O_{41}$ polycrystalline samples. (c) $\kappa_L$ and (d) $l_p$ of $Sr_{14-x}Y_xCu_{24}O_{41}$ polycrystalline samples. (e) Temperature-dependent $S$ of $Sr_{14-x}Y_xCu_{24}O_{41}$ polycrystalline samples, along the IP (in filled symbols) and OP (in empty symbols) directions. (f) Doping-dependent $S$ and $\kappa_M$ of $Sr_{14-x}Y_xCu_{24}O_{41}$ polycrystalline samples at 300 K.

To reveal the effect of Y-doping on the hole concentration in the spin ladder compounds, the $S$ of the polycrystalline samples was measured, as shown in Fig. 4(f). The values of $S$ along IP and OP directions in the same sample are very close. The positive value of $S$ indicates a p-type behavior in $Sr_{14-x}Y_xCu_{24}O_{41}$, which is expected for hole-doped spin ladders. Interestingly, the temperature dependence of $S$ changes as the doping level increases. For samples with x = 0, 1 and 2, $S$ decreases with increasing temperature, which is a typical non-degenerate semiconductor behavior.[45] In contrast, the samples with x = 4 and 6 exhibit a positive temperature dependence of $S$, which usually appears in metals and degenerate semiconductors.[45,46] A similar behavior has also been observed in the Ca-doped $Sr_{14-x}Ca_xCu_{24}O_{41}$, where Ca-doping transfers holes from chain to ladder layers, leading to an insulator-to-metal transition.[47] However, such a transition is unlikely to happen in the Y-doped spin ladder compounds since Y-doping usually reduces the hole concentration as reported by other

studies.[26,33] We believe the change in the scattering process is the origin for the different temperature dependence in the x = 4 and 6 samples. In conventional p-type semiconductor materials, $S$ is inversely related to the temperature and hole concentration, which can be expressed as:[48,49]

$$S = \frac{k_B}{e}\left[\frac{E_F - E_v}{k_B T} - (\mathrm{r} + 2.5)\right] \quad (3)$$

where $e$ is the charge of carrier, $E_F$ is the fermi energy, $E_v$ is the valence band energy, which is positively related to hole concentration, and r is the scattering factor, defined by the energy dependence of the mean scattering time of holes. As shown in Eq. (3), $S$ varies due to the scattering process of holes. The typical value of r is -0.5 for the acoustic phonon scattering and 1.5 for the ionized impurity scattering.[49,50] At low temperatures, the ionized impurity scattering due to Y-doping is the main scattering mechanism of holes.[50] However, as the temperature rises, the acoustic phonon scattering dominates the scattering mechanism, leading to a reduction of the scattering factor, which can change the temperature dependence of $S$.

The value of $S$ at 300 K increases as x increases from 0 to 4, which can be attributed to the change in hole concentration. $S$ starts to decrease for x = 6, indicating an increase of hole concentration in the heavily doped $Sr_{14-x}Y_xCu_{24}O_{41}$ due to the impurities. Using a single parabolic band (SPB) model,[51] the hole concentration of the samples can be estimated as $10 \times 10^{20}$, $8.0 \times 10^{20}$, $1.8 \times 10^{20}$, $1.2 \times 10^{20}$, and $8.3 \times 10^{20}$ $cm^{-1}$, for samples with x = 0, 1, 2, 4 and 6, respectively. The detailed analysis of the SPB model can be found in the Supplementary Material. Increasing the Y-doping level initially reduces the hole concentration until x = 4, then increases the hole concentration at x = 6. A possible explanation is that high Y-doping level leads to a higher number of lattice defects or formation of impurities, which may induce more holes. This increase can counterbalance the effect of the reduced population of $Cu^{3+}$ ions.[52] Another possible reason is that Y-doping, by shrinking the lattice constants like Ca-doping, can transfer holes from spin chains to ladders.[30]

As shown in Fig. 4(f), a similar Y-doping dependence can be observed on both $S$ and $\kappa_M$ of the polycrystalline samples at 300 K. It should be noted that the rates of change in $S$ and $\kappa_M$ are different. While both $S$ and $\kappa_M$ are dependent on the hole concentration, other mechanisms also play some roles. In the case of $\kappa_M$, both concentration and mobility of holes can determine the magnon-hole scattering process. In addition, the value of $\kappa_M$ is also influenced by magnon-defect scattering. Meanwhile, $S$ is predominantly governed by the hole concentration and acoustic phonon scattering at 300 K. Through the similar trends of $\kappa_M$ and $S$ as functions of doping level, the Y-doping effect on $\kappa_M$ in the spin ladder compounds is mainly attributed to the modulation of hole concentration and lattice distortion. In the lightly doped samples with x = 1 and 2, the Y-doping improves $\kappa_M$ by reducing the magnon-hole scattering, while in the heavily doped samples with x = 4 and 6, the Y-doping is not effective in increasing $\kappa_M$ due to the enhanced the magnon-defect and magnon-hole scattering. Due to the smaller ionic radius of Y than Sr, Y-doping can reduce the distance between the ladder layers and the (Sr, Y) layers, possibly leading to a mismatch between these layers and a bending in the $Cu-O-Cu$ coupling of the ladder layers.[28] In a previous study,[34] La -doping resulted in a monotonic increase of $\kappa_M$ with doping concentration, contrasting with the non-monotonic alteration of $\kappa_M$ observed in this study. Such a difference can be attributed to the smaller ionic radius of Y compared to La, resulting in a greater reduction of the *b*-axis and stronger magnon-defect scattering in Y-doped samples.

### C. Optical and thermal properties of single crystalline $Sr_{14-x}Y_xCu_{24}O_{41}$

Motivated by our findings on polycrystalline samples, we grew $Sr_{14-x}Y_xCu_{24}O_{41}$ single crystals through the TSFZ method, aiming to further enhance the magnon transport by reducing the defect and boundary scattering. Details on the structural characterization of single crystals can be found in the Supplementary Material. The Raman spectrum obtained from the single crystals is shown in Fig. 5. The broad two-magnon peak can be

detected in all three samples at the similar Raman shift of around 2800 $cm^{-1}$, which is consistent with the previous studies.[43,53] Two-magnon scattering originates from two magnons close to the Brillouin zone center with equal and opposite wavevector.[54] Since the two-magnon peak position is associated with the antiferromagnetic coupling energy in the ladder layer,[55] the similar peak position in all three samples indicates that the Y-doping does not observably affect the strength of the coupling energy. As a result, the magnon group velocity in the spin ladder is not changed noticeable by Y-doping. This result is consistent with the doping-independent lattice constants *a* and *c*. Since $Cu-O-Cu$ antiferromagnetic coupling only exists within the *ac*-plane, the nearly unchanged values for *a* and *c* by Y-doping have little effect on modifying the intralayer coupling energy.

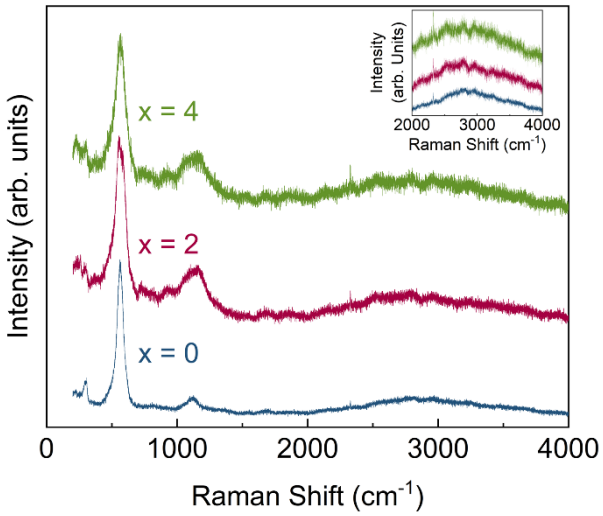


**Fig. 5**. Raman spectra of $Sr_{14-x}Y_xCu_{24}O_{41}$ single crystals. The inset is a zoomed-in view between 2000 and 4000 $cm^{-1}$ showing the two-magnon peak.

Fig. 6(a) shows the $\kappa$ of Y-doped single crystals, compared with that of undoped single crystals from a previous report.[17] It is noted that several groups have reported the $\kappa$ of $Sr_{14}Cu_{24}O_{41}$ single crystals,[17,18,22,28,34] as shown in Fig. S5 of the Supplementary Material. Overall, the reported $\kappa$ data along *c*-axis exhibit a similar trend. The peak value near 140 K shows a variation, which could be due to the differences in growth parameters and chemical stoichiometry. Nevertheless, the room-temperature $\kappa$ and $\kappa_M$ values remain largely consistent. Compared with the undoped sample along *c*-axis, the Y-doped samples have higher $\kappa$ values at room temperature while the $\kappa$ values at low temperatures are significantly suppressed. For comparison, the measured $\kappa$ perpendicular to *c*-axis shows a single peak near 20 K, indicating absence of magnon contribution. As shown in Fig. S6(a) of the Supplementary Material, it is noted that the measured $\kappa$ values perpendicular and parallel to *c*-axis are very close below 30 K, where phonon thermal transport dominates. As shown in Fig. 6(b), the single crystal samples exhibit higher $\kappa_M$ than the polycrystalline samples, which can be attributed to suppressed boundary and defect scattering caused by larger grain sizes and fewer lattice defects, respectively. Among the single crystal samples, $Sr_{12}Y_2Cu_{24}O_{41}$ exhibits the highest $\kappa_M$ of about 19 $W\,m^{-1}K^{-1}$ at 300 K, which is more than doubled compared with the undoped sample of about 7 $W\,m^{-1}K^{-1}$.[17] Both single crystalline and polycrystalline samples with x = 2 exhibit higher *S* values than those of undoped samples (Fig. S6(b)). Fig. 6(c) shows that the undoped single crystal, despite having a higher $l_M$ at low temperatures, suffers from a fast decline above 150 K, which is likely caused by the magnon-hole scattering.[19] It has been reported that the charge order temperature in $Sr_{14}Cu_{24}O_{41}$ is about 180 K.[56] Therefore, the magnon-hole scattering can be enhanced above this temperature, which can lead to the fast decline in $l_M$. The x = 4 sample has a lower $l_M$ compared with the x = 2 sample, which can be attributed to the enhanced magnon-defect due to the Y-induced lattice distortion.

The $C_p$ data of the samples are presented in Fig. S7 of the Supplementary Material. It has been found that the Y-doping shows a slightly enhancement on the Debye temperature and sound velocity in the spin ladder compounds. This enhancement is caused by the reduction of lattice parameter *b* as the interlayer bonding strength enhances with the smaller interlayer distance.[57] As a layered material, the Debye temperature and sound velocity of spin ladder compounds are dominated by the bonding strength within the *ac*-plane, as the phonon behavior is mainly defined by the intralayer phonon modes.[58] Thus, the reduction of the lattice constant *b* in interlayer direction causes weak impact on the Debye temperature and sound velocity. In the undoped spin ladder compound $Sr_{14}Cu_{24}O_{41}$, the long-range magnetic order is absent at finite temperatures in the spin ladder sublattice due to quantum fluctuations.[59,60] Ca-doping can lead to an antiferromagnetic ordering below 2.3 K.[60] However, according to our $C_p$ measurement, $Sr_{14-x}Y_xCu_{24}O_{41}$ samples do not exhibit any long-range magnetic ordering above 5 K.

Compared with the polycrystalline spin ladder compound $Sr_{14}Cu_{24}O_{41}$, $\kappa_M$ of the Y-doped single crystal $Sr_{12}Y_2Cu_{24}O_{41}$ is greatly increased by more than ten times at 300 K, as shown in Fig. 6(d). Firstly, utilizing the doping effect of Y, which can reduce the magnon-hole scattering, we are able to enhance $\kappa_M$ by 430% in the polycrystalline spin ladder compound. Furthermore, the single crystal $Sr_{12}Y_2Cu_{24}O_{41}$ sample exhibits a further enhanced $\kappa_M$, as a result of reduced defect and boundary scattering.

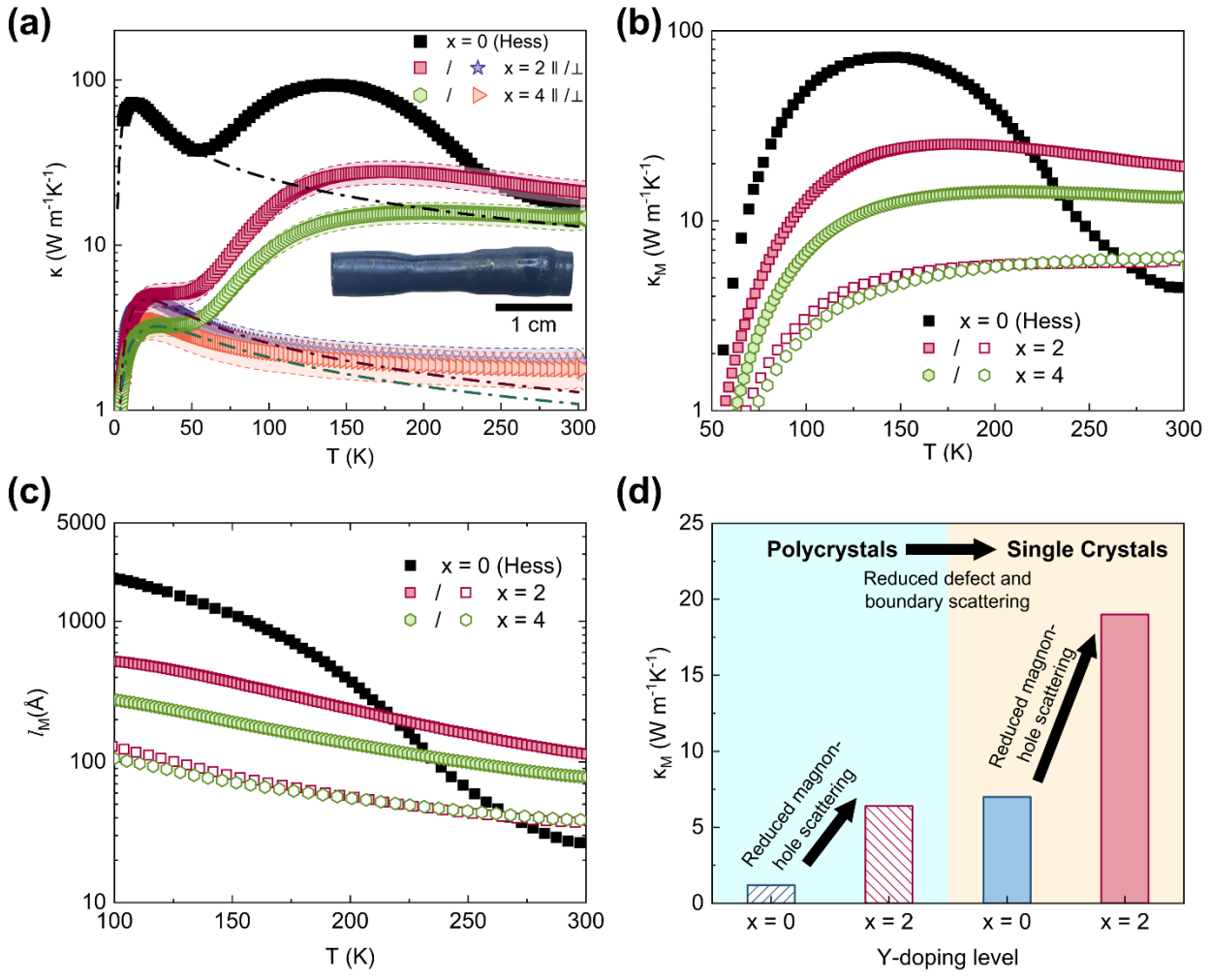


**Fig. 6**. (a) $\kappa$ of $Sr_{14-x}Y_xCu_{24}O_{41}$ single crystals measured parallel and perpendicular to *c*-axis, respectively. Shown for comparison is the $\kappa$ for $Sr_{14}Cu_{24}O_{41}$ along the *c*-axis reported by Hess *et al.*[17] The dashed lines in (a) are fitted $\kappa_L$ by the Callaway model.[42]

The shaded area represents the uncertainty of the measurement. The inset in (a) is a photo of a $Sr_{12}Y_2Cu_{24}O_{41}$ single crystal grown by the TSFZ method. (b) $\kappa_M$ and (c) $l_M$ of $Sr_{14-x}Y_xCu_{24}O_{41}$ single crystals (in solid symbols) compared with the polycrystal data (in open symbols) and literature values.[17] (d) The comparison of $\kappa_M$ of $Sr_{14-x}Y_xCu_{24}O_{41}$ with x = 0 and 2 at 300 K. The $\kappa_M$ data of single crystal sample with x = 0 is calculated using the $\kappa$ reported by Hess *et al.*[17]

## IV. CONCLUSIONS

We investigate the effect of Y-doping on the thermal transport properties of magnons in both polycrystalline and single crystalline spin ladder compounds, $Sr_{14-x}Y_xCu_{24}O_{41}$. The Y-doping effect on $\kappa_M$ exhibits a non-monotonic behavior. Due to its higher valence state, Y-doping can effectively reduce the hole concentration and magnon-hole scattering in the lightly doped polycrystalline samples. Consequently, both $\kappa_M$ and $S$ of $Sr_{12}Y_2Cu_{24}O_{41}$, are enhanced compared with the undoped sample at room temperature. Further increasing the Y-doping level induces lattice distortion, which intensifies magnon-defect scattering, leading to negligible changes and eventual suppression of $\kappa_M$ and $S$. This behavior differs from the monotonic increase of $\kappa_M$ in La-doped spin ladders,[34] attributed to stronger magnon-defect scattering in Y-doped samples with shorter spacing between spin ladders and (Sr, Y) layers. The Y-doping also leads to a change of the temperature dependence on $S$ away from the conventional behavior of non-degenerate semiconductors, due to stronger ionized impurity scattering at low temperatures. The location of the two-magnon Raman peak, which is independent of Y-doping level, indicates little modification of the magnon group velocity through Y-doping. In the single crystal samples, $\kappa_M$ is further enhanced by minimizing defect and boundary scattering. The single crystal of $Sr_{12}Y_2Cu_{24}O_{41}$ exhibits a large room-temperature $\kappa_M$ of 19 $W\,m^{-1}K^{-1}$, which is more than ten times greater than that of the undoped polycrystalline sample. Additionally, Y-doping monotonically suppresses $\kappa_L$ and $l_p$ due to the enhanced phonon-defect scattering. This work reveals the interplay between magnon-hole scattering and magnon-defect scattering in modifying magnon thermal conductivity, which can provide useful guidelines for designing magnetic materials with controlled magnon properties for energy transport and quantum information processing.

## SUPPLEMENTARY MATERIAL

See the supplementary material for the uncertainty analysis for the thermal conductivity measurements, the phase analysis and structure characterization of samples, the grain size distribution of polycrystalline samples, the thermal property analysis with Callaway model, the thermal conductivity data of single crystals from previous studies, and Seebeck coefficient and specific heat data for single crystals.


## ACKNOWLEDGEMENTS

This work was supported by the National Science Foundation (grant No. 2144328).


## AUTHOR DECLARATIONS

### Conflict of Interest

The authors have no conflicts to disclose.

### Author Contributions

Shuchen Li and Shucheng Guo contributed equally to this work.

**Shuchen Li:** Conceptualization (equal); Formal analysis (equal); Investigation (equal); Writing – original draft (equal); Writing – review & editing (equal). **Shucheng Guo:** Formal analysis (equal); Investigation (equal); Writing – original draft (equal); Writing – review & editing (equal). **Yitian Wang:** Investigation (equal); Writing – review & editing (support). **Hongze Li:** Investigation (equal); Writing – review & editing (support). **Youming Xu:** Investigation (support); Writing – review & editing (support). **Veronica Carta:** Investigation (support); Writing – review & editing (support). **Jianshi Zhou:** Supervision (equal); Investigation (equal); Writing – review & editing (support). **Xi Chen:** Conceptualization (lead); Supervision (lead); Funding acquisition (lead); Writing – review & editing (equal)

## DATA AVAILABILITY

The data that support the findings of this study are available from the corresponding author upon reasonable request.

## REFERENCES


[1] C. Kittel, and P. McEuen, *Introduction to Solid State Physics* (John Wiley & Sons, 2018).

[2] S. Guo, Y. Xu, T. Hoke, G. Sohi, S. Li, and X. Chen, J Appl Phys **133**(12), (2023).

[3] B. Lüthi, Journal of Physics and Chemistry of Solids **23**(1), 35–38 (1962).

[4] N. Terakado, Y. Nara, Y. Machida, Y. Takahashi, and T. Fujiwara, Sci Rep **10**(1), 14468 (2020).

[5] X. Zhao, J.C. Wu, and Z.Y. Zhao, Appl. Phys. Lett **108**, 242405 (2016).

[6] H. Nakayama, B. Xu, S. Iwamoto, K. Yamamoto, R. Iguchi, A. Miura, T. Hirai, Y. Miura, Y. Sakuraba, J. Shiomi, and K. Uchida, Appl Phys Lett **118**(4), (2021).

[7] K. Uchida, S. Takahashi, K. Harii, J. Ieda, W. Koshibae, K. Ando, S. Maekawa, and E. Saitoh, Nature **455**(7214), 778–781 (2008).

[8] K. Vandaele, S.J. Watzman, B. Flebus, A. Prakash, Y. Zheng, S.R. Boona, and J.P. Heremans, Materials Today Physics **1**, 39–49 (2017).

[9] A. V. Chumak, V.I. Vasyuchka, A.A. Serga, and B. Hillebrands, Nat Phys **11**(6), 453–461 (2015).

[10] T. Jungwirth, X. Marti, P. Wadley, and J. Wunderlich, Nat Nanotechnol **11**(3), 231–241 (2016).

[11] A. V. Chumak, A.A. Serga, and B. Hillebrands, Nat Commun **5**(1), 4700 (2014).

[12] S.R. Boona, and J.P. Heremans, Phys Rev B **90**(6), 64421 (2014).

[13] B. Khodadadi, A. Rai, A. Sapkota, A. Srivastava, B. Nepal, Y. Lim, D.A. Smith, C. Mewes, S. Budhathoki, A.J. Hauser, M. Gao, J.-F. Li, D.D. Viehland, Z. Jiang, J.J. Heremans, P.V. Balachandran, T. Mewes, and S. Emori, Phys Rev Lett **124**(15), 157201 (2020).

[14] Q. Sun, S. Hou, B. Wei, Y. Su, V. Ortiz, B. Sun, J.Y.Y. Lin, H. Smith, S. Danilkin, D.L. Abernathy, R. Wilson, and C. Li, Materials Today Physics **35**, 101094 (2023).

[15] S. Guo, H. Li, X. Bai, Y. Wang, S. Li, R.E. Dunin-Borkowski, J. Zhou, and X. Chen, Cell Rep Phys Sci **5**(3), 101879 (2024).

[16] X. Wu, Z. Liu, and T. Luo, J Appl Phys **123**(8), (2018).

[17] C. Hess, C. Baumann, U. Ammerahl, B. Büchner, F. Heidrich-Meisner, W. Brenig, and A. Revcolevschi, Phys Rev B **64**(18), 184305 (2001).

[18] A. V Sologubenko, K. Giannó, H.R. Ott, U. Ammerahl, and A. Revcolevschi, Phys Rev Lett **84**(12), 2714–2717 (2000).

[19] C. Hess, H. ElHaes, B. Büchner, U. Ammerahl, M. Hücker, and A. Revcolevschi, Phys Rev Lett **93**(2), 027005 (2004).

[20] T. Siegrist, L.F. Schneemeyer, S.A. Sunshine, J. V Waszczak, and R.S. Roth, Mater Res Bull **23**(10), 1429–1438 (1988).

[21] J. Etrillard, M. Braden, A. Gukasov, U. Ammerahl, and A. Revcolevschi, Physica C Supercond **403**(4), 290–296 (2004).

[22] X. Chen, D. Bansal, S. Sullivan, D.L. Abernathy, A.A. Aczel, J. Zhou, O. Delaire, and L. Shi, Phys Rev B **94**(13), 134309 (2016).

[23] S. Gopalan, T.M. Rice, and M. Sigrist, Phys Rev B **49**(13), 8901–8910 (1994).

[24] X. Zhao, Z. Zhao, X. Liu, X. Sun, X. Zhao, Z.Y. Zhao, and X.G. Liu, Sci. China-Phys. Mech. Astron **59**, 117501 (2016).

[25] X. Chen, K. Jarvis, S. Sullivan, Y. Li, J. Zhou, and L. Shi, Phys Rev B **95**(14), 144310 (2017).

[26] N. Nücker, M. Merz, C.A. Kuntscher, S. Gerhold, S. Schuppler, R. Neudert, M.S. Golden, J. Fink, D. Schild, S. Stadler, V. Chakarian, J. Freeland, Y.U. Idzerda, K. Conder, M. Uehara, T. Nagata, J. Goto, J. Akimitsu, N. Motoyama, H. Eisaki, S. Uchida, U. Ammerahl, and A. Revcolevschi, Phys Rev B **62**(21), 14384–14392 (2000).

[27] M. Hücker, V. Kataev, J. Pommer, J. Harraß, A. Hosni, C. Pflitsch, R. Gross, and B. Büchner, Phys Rev B **59**(2), R725–R728 (1999).

[28] K. Naruse, T. Kawamata, M. Ohno, Y. Matsuoka, K. Kumagai, and Y. Koike, Solid State Commun **154**, 60–63 (2013).

[29] G. Deng, D.M. Radheep, R. Thiyagarajan, E. Pomjakushina, S. Wang, N. Nikseresht, S. Arumugam, and K. Conder, J Cryst Growth **327**(1), 182–188 (2011).

[30] G. Deng, V. Pomjakushin, V. Petříček, E. Pomjakushina, M. Kenzelmann, and K. Conder, Phys Rev B **84**(14), 144111 (2011).

[31] S. Li, S. Guo, Y. Xu, J. Zhou, and X. Chen, ACS Appl Electron Mater **4**(2), 787–794 (2022).

[32] K. Kudo, S. Ishikawa, T. Noji, T. Adachi, Y. Koike, K. Maki, S. Tsuji, and K. Kumagai, J Low Temp Phys **117**(5), 1689–1693 (1999).

[33] T. Osafune, N. Motoyama, H. Eisaki, and S. Uchida, Phys Rev Lett **78**(10), 1980–1983 (1997).

[34] K. Kudo, S. Ishikawa, T. Noji, T. Adachi, Y. Koike, K. Maki, S. Tsuji, and K. Kumagai, J Physical Soc Japan **70**(2), 437–444 (2001).

[35] A. Revcolevschi, U. Ammerahl, and G. Dhalenne, J Cryst Growth **198–199**, 593–599 (1999).

[36] D.M. de Leeuw, C.A.H.A. Mutsaers, G.P.J. Geelen, H.C.A. Smoorenburg, and C. Langereis, Physica C Supercond **152**(5), 508–512 (1988).

[37] A.R. Denton, and N.W. Ashcroft, Phys Rev A (Coll Park) **43**(6), 3161–3164 (1991).

[38] D. Matsunaka, E.T. Rodulfo, and H. Kasai, Solid State Commun **134**(5), 355–360 (2005).

[39] W. Fei, X. Sishen, C. Zhan, and L. Jingkui, J Mater Sci **27**(11), 3082–3084 (1992).

[40] M. Kato, T. Adachi, and Y. Koike, Physica C Supercond **265**(1), 107–112 (1996).

[41] C. Hess, Phys Rep **811**, 1–38 (2019).

[42] J. Callaway, Physical Review **113**(4), 1046–1051 (1959).

[43] X. Chen, J. Kim, Q. Jia, S.E. Sullivan, Y. Xu, K. Jarvis, J. Zhou, and L. Shi, Adv Funct Mater **30**(30), 2001637 (2020).

[44] A.D. McConnell, S. Uma, and K.E. Goodson, Journal of Microelectromechanical Systems **10**(3), 360–369 (2001).

[45] M.W. Heller, and G.C. Danielson, Journal of Physics and Chemistry of Solids **23**(6), 601–610 (1962).

[46] X. Chen, S.N. Girard, F. Meng, E. Lara-Curzio, S. Jin, J.B. Goodenough, J. Zhou, and L. Shi, Adv Energy Mater **4**(14), 1400452 (2014).

[47] W. Qing-Bo, X. Xiang-Fan, T. Qian, W. Hong-Tao, and X. Zhu-An, Chinese Physics Letters **25**(5), 1857–1860 (2008).

[48] D.Michael. Rowe, *Thermoelectrics Handbook : Macro to Nano* (CRC/Taylor & Francis, 2006).

[49] L. Su, H. Shi, S. Wang, D. Wang, B. Qin, Y. Wang, C. Chang, and L. Zhao, Adv Energy Mater **13**(18), (2023).

[50] K. Alfaramawi, The European Physical Journal Plus **126**(1), 8 (2011).

[51] X. Chen, C. Li, Y. Xu, A. Dolocan, G. Seward, A. Van Roekeghem, F. Tian, J. Xing, S. Guo, N. Ni, Z. Ren, J. Zhou, N. Mingo, D. Broido, and L. Shi, Chemistry of Materials **33**(17), 6974–6982 (2021).

[52] Z. Liu, J. Mao, J. Sui, and Z. Ren, Energy Environ Sci **11**(1), 23–44 (2018).

[53] M. V Abrashev, C. Thomsen, and M. Surtchev, Physica C Supercond **280**(4), 297–303 (1997).

[54] A. Gozar, G. Blumberg, B.S. Dennis, B.S. Shastry, N. Motoyama, H. Eisaki, and S. Uchida, Phys Rev Lett **87**(19), 197202 (2001).

[55] S. Sugai, T. Shinoda, N. Kobayashi, Z. Hiroi, and M. Takano, Phys Rev B **60**(10), R6969–R6972 (1999).

[56] M. Braden, J. Etrillard, A. Gukasov, U. Ammerahl, and A. Revcolevschi, Phys Rev B **69**(21), 214426 (2004).

[57] H. Zabel, Journal of Physics: Condensed Matter **13**(34), 7679–7690 (2001).

[58] A.A. Balandin, and D.L. Nika, Materials Today **15**(6), 266–275 (2012).

[59] R. Eder, Phys Rev B **57**(20), 12832–12840 (1998).

[60] T. Nagata, H. Fujino, K. Satoh, N. Yamamori, J. Akimitsu, S. Katano, M. Nishi, K. Kakurai, M. Hiroi, M. Sera, N. Kobayashi, K. Tenya, H. Amitsuka, T. Takigawa, H. Inago, and T. Sakakibara, J Physical Soc Japan **70**(8), 2419–2424 (2001).